**ARTICLE**

**Open Access**

# Gain enhancement of perovskite nanosheets by a patterned waveguide: excitation and temperature dependence of gain saturation

Inhong Kim[1], Ga Eul Choi[1], Ming Mei[1], Min Woo Kim[1], Minju Kim[1], Young Woo Kwon[2], Tae-In Jeong[1], Seungchul Kim[1], Suck Won Hong[1✉], Kwangseuk Kyhm[1✉] and Robert A. Taylor[3✉]

## Abstract

Optical gain enhancement of two-dimensional $CsPbBr_3$ nanosheets was studied when the amplified spontaneous emission is guided by a patterned structure of polyurethane-acrylate. Given the uncertainties and pitfalls in retrieving a gain coefficient from the variable stripe length method, a gain contour $g(\hbar\omega, x)$ was obtained in the plane of spectrum energy ($\hbar\omega$) and stripe length ($x$), whereby an average gain was obtained, and gain saturation was analysed. Excitation and temperature dependence of the gain contour show that the waveguide enhances both gain and thermal stability due to the increased optical confinement and heat dissipation, and the gain origins were attributed to the two-dimensional excitons and the localized states.

## Introduction

Metal halide perovskites (MHPs) show many outstanding features such as low-cost solution processability, precise bandgap tunability over the entire visible spectral range, and high quantum yield[1,2], and these advantages can be used in a broad range of applications such as solar cells[3,4], light-emitting diodes[5,6], lasers[7–13], and photodetectors[14,15]. Although organic-inorganic perovskites were studied a great deal, all inorganic perovskites were found to be superior in terms of thermal stability and moisture sensitivity[16,17].

In particular, MHPs are considered a promising laser medium. In the case of organic-inorganic perovskites such as $MAPbI_3$ film, it was reported that a narrow amplified spontaneous emission (ASE) feature emerges near the threshold ($\sim46\,\mu Jcm^{-2}$), and the gain was observed to be $200\,cm^{-1}$ at room temperature under excitation fluence of $100\,\mu Jcm^{-2}$ (see ref. [18]). On the other hand, all inorganic perovskite $CsPbBr_3$ film is known to have a large number of defects in its polycrystalline morphology. Recently, this obstacle was resolved by a large scale single-crystal film of $CsPbBr_3$, where a low threshold ($\sim24\,\mu Jcm^{-2}$) was observed, and the gain was measured to be up to $1369 \pm 101\,cm^{-1}$ with an excitation fluence of $\sim720\,\mu Jcm^{-2}$ [10]. $CsPbBr_3$ film with small ($\sim200\,nm$) grains was also seen to exhibit a large gain coefficient ($\sim10^4\,cm^{-1}$) when the excited carrier density is similar to the Mott density ($\sim10^{19}\,cm^{-3}$)[19].

In $CsPbBr_3$ quantum dots (QDs), the Auger process becomes dominant due to the strong confinement, and the excess energy of a photo-excited electron-hole pair is likely to be converted to multi-excitons via carrier-multiplication. As a result, biexcitons are known to play a crucial role for the intrinsic material gain ($g_m$) in $CsPbBr_3$ QDs[20]. However, the Auger process also shortens the decay time for the population inversion. In the case of colloidal CdSe QDs, the graded potential structure of multi-layered thick shells is used to suppress the Auger

Correspondence: Suck Won Hong (swhong@pusan.ac.kr) or
Kwangseuk Kyhm (kskyhm@pusan.ac.kr) or
Robert A. Taylor (robert.taylor@physics.ox.ac.uk)
[1]Department of Opto & Cogno Mechatronics Engineering, RCDAMP, Pusan National University, Busan 46241, Republic of Korea
[2]Department of Nano-Fusion Technology, Pusan National University, Busan 46241, Republic of Korea
Full list of author information is available at the end of the article
These authors contributed equally: Inhong Kim, Ga Eul Choi, Ming Mei

process, whereby electrically pumped ASE was successfully demonstrated[21]. Unfortunately, the Auger recombination time in $CsPbBr_3$ QDs is known to be shorter than that in CdSe QDs[22]. Therefore, the gain is limited by the inherent nature of the perovskite material. $CsPbBr_3$ nanosheets are expected to be less vulnerable to Auger processes due to their two-dimensional (2D) nature[23,24], and the fast in-plane charge transport[25] is also advantageous for electrically pumped lasers. So far, no gain study has been reported in $CsPbBr_3$ nanosheets.

Alternatively, the optical confinement factor ($\gamma$) can be enhanced by waveguide geometry, plasmonic waveguides, and refractive index matching, resulting in an increase of net gain ($g = \gamma g_m - \alpha$) despite the limits of small material gain ($g_m$) and loss ($\alpha$). In the case of $CsPbBr_3$ nanostructures, most interest is focused on material gain, and the waveguide effect was rarely studied[26,27]. As evidence of stimulated emission, an emergence of superlinear emission intensity growth and spectral narrowing are often shown with increasing excitation intensity[7-13]. However, a gain coefficient is necessary for a quantitative evaluation of the light amplification at a particular emission wavelength. A gain spectrum is also important to allow a determination of the energetic distribution of population inversion, whereby the microscopic origin of the gain can be revealed. When a gain is present, the ASE intensity shows an exponential increase as the propagation length increases, otherwise spontaneous emission gives rise to a linear increase with stripe length. Therefore, an optical gain coefficient at a particular wavelength can be obtained through the stripe length-dependent ASE intensity, which is known as the variable stripe length method (VSLM)[28].

The VSLM is widely used for its simplicity, and most of the modal gain studies on MHPs have been based on the VSLM. However, various uncertainties can be involved when an optical gain coefficient is retrieved from the stripe length dependence of the ASE. These are very important to obtain a consistent gain coefficient, but usually overlooked. Therefore, possible pitfalls in both experimental implementation and numerical retrieval of $g$ should be considered[18,26,29]. For example, the intensity uniformity should be confirmed over the whole optical stripe, which is obtained from a Gaussian laser distribution using a cylindrical lens. An upper limit for the stripe length should be known for fitting due to the gain saturation. A threshold stripe length for amplification should also be considered when the stripe length is comparable to the stripe width.

In this work, we have studied the net gain of $CsPbBr_3$ nanosheets in terms of temperature and excitation dependence, gain saturation, and the waveguide effect. We address possible pitfalls and limits of the old analysis in the VSLM; our stripe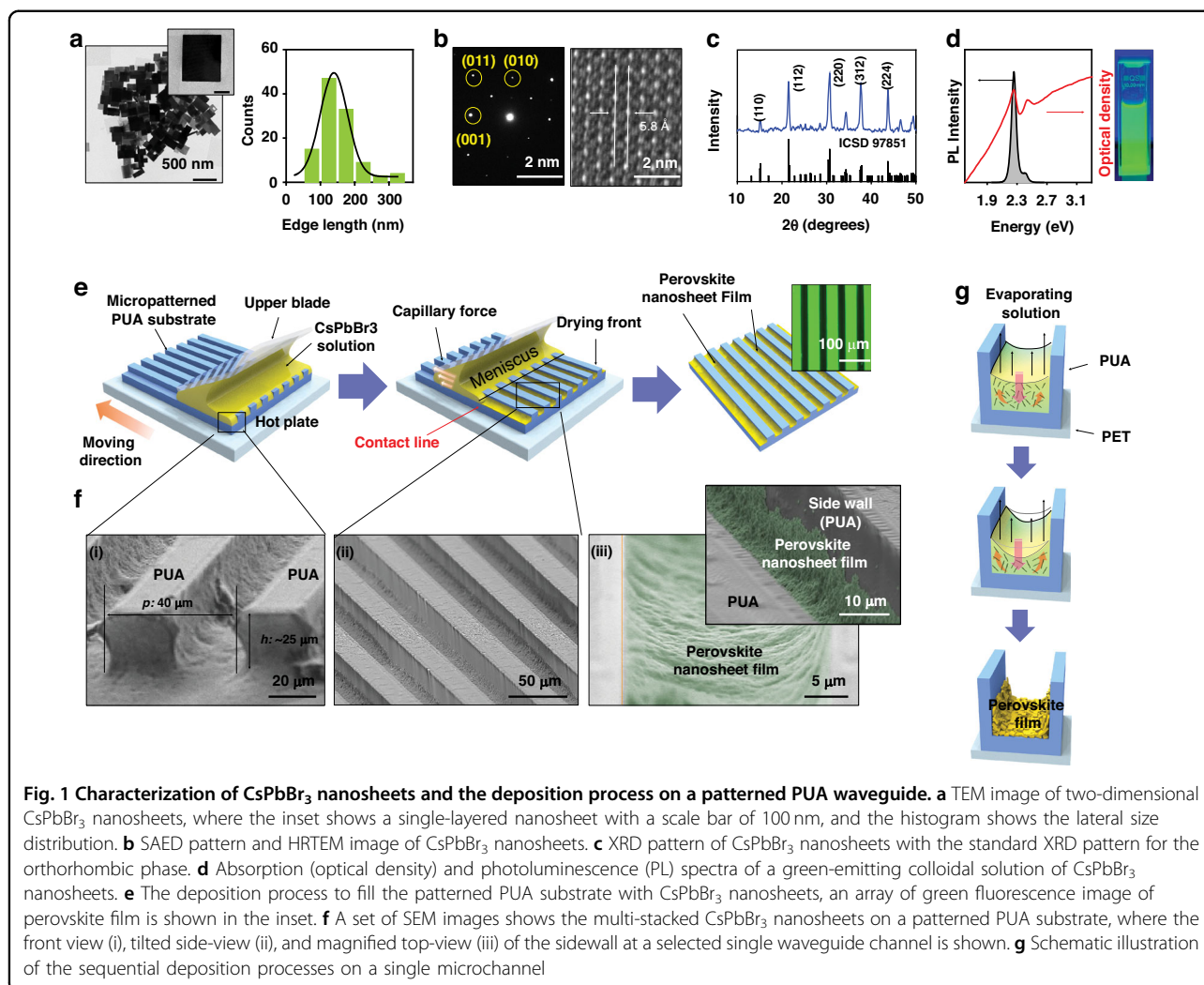 length-dependent gain coefficient $g(x)$ was estimated at a particular emission energy ($\hbar\omega$), whereby we obtained a spectrum-length gain contour $g(\hbar\omega, x)$. We found $g(\hbar\omega, x)$ is quite useful in evaluating the gain saturation as a function of temperature and excitation intensity, whereby a representative average gain can be obtained. Additionally, we have also confirmed an enhancement of the modal gain in $CsPbBr_3$ nanosheets through a micron scale waveguide structure, which was produced by a patterned substrate of polyurethane-acrylate (PUA).

## Results

In Fig. 1a–f, the characterization of $CsPbBr_3$ nanosheets and a schematic of the deposition process on a patterned PUA waveguide are shown, whereby a periodic array of perovskite stripes was obtained. As a first step, $CsPbBr_3$ nanosheets were synthesized by a well-established hot injection method (see "Materials and methods"). Briefly, Cesium-oleate was used as a precursor, which accelerates the lateral growth of perovskite nanosheets with a high yield. To stabilize the colloidal solution of the two-dimensional (2D) nanosheets, oleic acid and oleylamine were used, where short carbon ligands (octanoic acid and octylamine) were combined to inhibit the uncontrolled vertical growth and stabilize the lateral growth mode in 2D nanosheets.

Figure 1a shows a transmission electron microscopy (TEM) image and a histogram of the lateral size distribution, where the inset TEM image clearly displays an isolated single $CsPbBr_3$ nanosheet with a square shape, and we obtained the average lateral size to be ($\sim 140 \pm 40$ nm). To determine the crystallinity of the nanosheets, a selected area electron diffraction (SAED) pattern and a high-resolution TEM (HRTEM) image were measured. The SAED pattern (Fig. 1b) indicates an orthorhombic crystal phase (ICSD 97851, Pbnm (62), $a = 8.207$ A, $b = 8.255$ A, $c = 11.759$ A), and the lattice fringe of 5.8 A was confirmed by the HRTEM image. XRD measurements were also conducted to determine the crystallinity of perovskite nanosheets (Fig. 1c). Based on the obtained diffraction patterns, the diffraction peaks were located at 15.16°, 21.46°, and 30.24°, which were matched with the (110), (112), and (220) crystal planes. It can be inferred that the perovskite nanosheets have an orthorhombic crystal structure, as the first three strong peaks, namely, (110), (112) and (220), together with the lattice fringe (5.8 A)matched well with the standard orthorhombic perovskite structure[30].

In Fig. 1d, absorption and PL spectra were measured with a $CsPbBr_3$ nanosheet solution in a hexane solvent, which shows a green image under UV lamp excitation. Compared with the absorption peak at the lowest energy ($\sim 2.357$ eV), the PL spectrum shows a narrow linewidth ($\sim 17$ nm) without a low energy spectral tail. Therefore, the PL at room temperature can be attributed to 2D

**Fig. 1 Characterization of CsPbBr₃ nanosheets and the deposition process on a patterned PUA waveguide. a** TEM image of two-dimensional CsPbBr₃ nanosheets, where the inset shows a single-layered nanosheet with a scale bar of 100 nm, and the histogram shows the lateral size distribution. **b** SAED pattern and HRTEM image of CsPbBr₃ nanosheets. **c** XRD pattern of CsPbBr₃ nanosheets with the standard XRD pattern for the orthorhombic phase. **d** Absorption (optical density) and photoluminescence (PL) spectra of a green-emitting colloidal solution of CsPbBr₃ nanosheets. **e** The deposition process to fill the patterned PUA substrate with CsPbBr₃ nanosheets, an array of green fluorescence image of perovskite film is shown in the inset. **f** A set of SEM images shows the multi-stacked CsPbBr₃ nanosheets on a patterned PUA substrate, where the front view (i), tilted side-view (ii), and magnified top-view (iii) of the sidewall at a selected single waveguide channel is shown. **g** Schematic illustration of the sequential deposition processes on a single microchannel

excitons confined in nanosheets with large lateral size (80 ∼ 300 nm) and thin thickness (7–15 nm), when the exciton Bohr radius ($a_x$ ∼3.6 nm) and the binding energy ($E_x^b$ ∼ 40 meV) of bulk CsPbBr₃ are considered[31]. Near the ground state absorption peak of CsPbBr₃ nanostructures, two fine peaks have been shown to exist with a splitting energy of ∼60 meV due to the electron-heavy hole (HH) and electron-light hole (LH) states[32]. In our case, they are too broad to be resolved from the absorption peak at ∼2.357 eV. On the other hand, both absorption and PL spectra show a secondary peak near ∼2.54 eV, which is separated by ∼183 meV from the lowest peak. This can be explained by a bi-modal thickness distribution[33]; recent work reported that colloidal single crystal CsPbBr₃ per-ovskite nanosheets with large lateral sizes (up to a few µm) and thickness of a few unit cells size (<5 nm) can be synthesized by introducing short and long ligands. When the volumetric ratio of short to long ligands was 0.67 in the perovskite solution, the mean lateral size of large nanosheets was ∼5.16 µm. In the PL spectrum of the large

nanosheets, two distinct peaks at 458 nm and 491 nm were also observed, which can be attributed to a bi-modal thickness distribution.

Figure 1e shows the sequential deposition process on a patterned structure, where the periodic microchannels were filled with a solution of CsPbBr₃ nanosheets. Because the substrate consists of patterned PUA on polyethylene terephthalate (PET) film, the trapped CsPbBr₃ nanosheets were stacked only on the trench of the microstructure, partially wetting on the sidewall of PUA, except the mesa areas. Therefore, light propagation along the channels can be guided, and the lateral light propagation can be amplified due to the enhanced optical confinement. The detailed photo- and nanoimprint-lithography for the micropatterned waveguides are explained in the Supple-mentary Information. We used capillary-directed self-assembly by employing a motorized translation stage (i.e., programmable moving substrate)[34], where an inclined upper blade traps and sweeps the receding meniscus of the colloidal solution across the micropatterned substrate.

The meniscus-assisted solution deposition process is known to yield a high coverage over a large area. Since we used a micropatterned structure instead of a flat substrate, the engraved channels confined the $CsPbBr_3$ nanosheet solution. As shown in the middle panel of Fig. 1e, the trapped meniscus of the nanosheet solution quickly flows through the microfluidic channels, which is driven by capillary force and repetitive physical deposition. We found that the production yield of a uniformly stacked film of $CsPbBr_3$ nanosheets was sensitive to the number of the deposition processes and the surrounding temperature as it is associated with the evaporation rate of the solution. Therefore, the temperature was carefully fixed at 60 °C for constant growth of $CsPbBr_3$ nanosheets since the boiling point of the solvent (i.e., anhydrous hexane) is 69 °C and the nonvolatile solute (i.e., $CsPbBr_3$ nanosheets) undergoes an unwanted phase transition. For complete evaporation of the solvent and simultaneous annealing, the patterned substrate (PUA/PET) was placed on a hot plate in a pre-heated state at 60 °C. After repetitive deposition processes (20 times) with multiple supplies of the nanosheet solution, an array of the nanosheet stripes separated by the PUA walls was obtained on a large scale ($4 \times 4$ cm$^2$). The right panel inset of Fig. 1e shows a clear fluorescence image of the $CsPbBr_3$ nanosheet stripes. Therefore, light amplification is expected along each stripe efficiently.

Figure 1f shows scanning electron microscope (SEM) images of the micropatterned PUA structure, and the cross section in Fig. 1f(i) shows a 1:1 aspect ratio. Given the periodic micropatterned channels (40 µm) in Fig. 1f(ii), a conformal coating of $CsPbBr_3$ nanosheets was successfully obtained only on the engraved trench areas as shown in Fig. 1f(iii). A highly magnified SEM image in Fig. 1f(iii) indicates that the closely packed $CsPbBr_3$ nanosheets partially wet the surface of the PUA side walls by a conformally stacked layer. Therefore, our rapid assembly strategy is highly advantageous for producing spatially arranged multi-stacked perovskite nanosheets for a micro-laser array. It is also noteworthy that the generation of a micropatterned perovskite film is highly reproducible with a help of conventional lithographic techniques and capillary-directed self-assembly using simple organic solvent evaporation.

Figure 1g shows the sequential deposition process for the $CsPbBr_3$ nanosheets on a single microchannel. When an aqueous $CsPbBr_3$ nanosheets suspension was deposited, the volatile hexane solvent transported the nonvolatile solute of $CsPbBr_3$ nanosheets into the trench area in a strictly controlled geometry by the fixed upper glass blade and the moving substrate. At this moment, all the solutes can be deposited and effectively trapped only on the trench area by the favorable surface wetting along with the lateral sliding of the meniscus, facilitating a

highly diluted solution concentration level ($C \sim 0.5$ µg mL$^{-1}$) (Supplementary Information). The consequent receding contact line is swept by a physical dragging force on the mesa surface and spontaneous solvent evaporation in the microfluidic channels, where the hydrodynamic flows and evaporative flux strictly drive the nanosheets into the trench area (middle panel in Fig. 1g)[35]. Given the largely reduced meniscus over the patterned substrate, the liquid thin film is continuously filled, and the nonvolatile solutes can be positioned in the deep grooved area (i.e., trench). On the other hand, the multiple supplies of the solution prohibit discontinuous patterned film formation by the coffee ring effect[36]. We intentionally applied a highly diluted solution in this process to optimize the thickness level of the nanosheets. With this effective guidance of the micropatterned substrate, the nanosheets were continuously deposited at the receding contact line at the air-liquid-solid interface, thereby anchored at each narrow microfluidic channel at the final stage of the complete solvent evaporation (the lower panel in Fig. 1g).
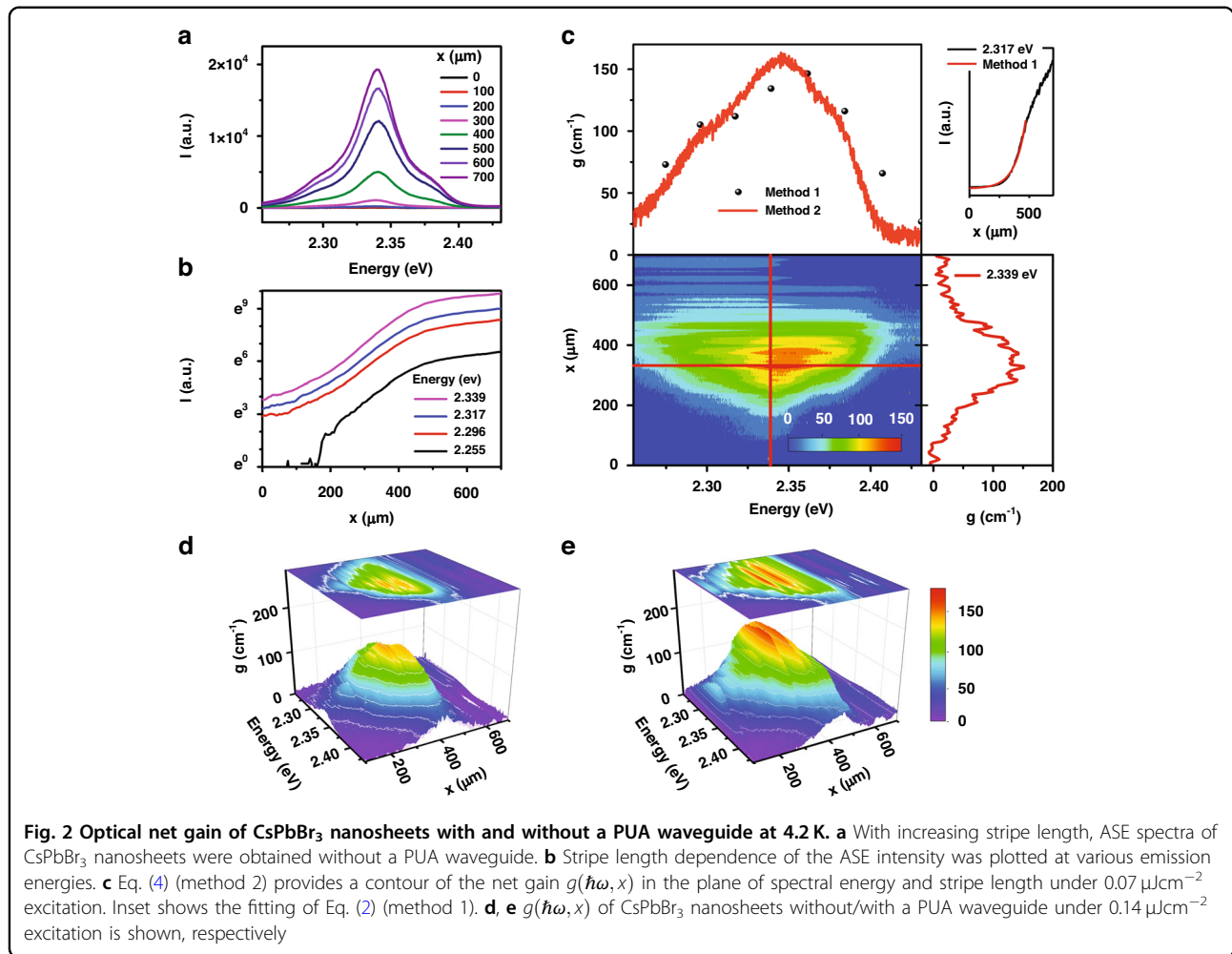
In Fig. 2, we show the net gain of $CsPbBr_3$ nanosheets with and without a PUA waveguide using the VSLM (Supplementary Information). Figure 2a shows the ASE spectra of $CsPbBr_3$ nanosheets on PET without a PUA waveguide with increasing stripe length. Whilst the ASE propagates along an excited stripe towards the sample edge, the ASE intensity $I(\hbar\omega, x)$ becomes amplified by a net gain coefficient $g$, which consists of an optical confinement factor $\gamma$, an intrinsic material gain $g_m$, and a propagation loss $\alpha$, i.e., $g = \gamma g_m - \alpha$. Additionally, spontaneous emission is also involved with a spontaneous emission density $J_{sp}(\hbar\omega)$ and solid angle $\Omega$. Therefore, the stripe length dependence of the ASE intensity is given by:

$$\frac{dI(\hbar\omega, x)}{dx} = g(\hbar\omega)I(\hbar\omega, x) + J_{sp}(\hbar\omega)\Omega \qquad (1)$$

When stripe lengths are short, the gain coefficient is assumed to be independent to stripe length. Therefore, the solution to Eq. (1) is given by:

$$I(\hbar\omega, x) = \frac{J_{sp}(\hbar\omega)\Omega}{g(\hbar\omega)} \left( e^{g(\hbar\omega)x} - 1 \right) \qquad (2)$$

In Fig. 2b, the ASE intensity with stripe length $I(x)$ at various emission energies $\hbar\omega$ is shown. As the measured $I(x)$ shows an exponential increase $\sim e^{gx}$ up to $\lesssim 500$ µm, a net gain coefficient can be obtained by fitting. For example, the ASE intensity selected at 2.317 eV (inset of Fig. 2c) fits well with Eq. (2) up to ~500 µm, giving rise to a gain coefficient of 112 cm$^{-1}$. Alternatively, the two ASE intensities at $x$ and $2x$ can be used instead of fitting.

**Fig. 2 Optical net gain of CsPbBr$_3$ nanosheets with and without a PUA waveguide at 4.2 K. a** With increasing stripe length, ASE spectra of CsPbBr$_3$ nanosheets were obtained without a PUA waveguide. **b** Stripe length dependence of the ASE intensity was plotted at various emission energies. **c** Eq. (4) (method 2) provides a contour of the net gain $g(\hbar\omega, x)$ in the plane of spectral energy and stripe length under 0.07 μJcm$^{-2}$ excitation. Inset shows the fitting of Eq. (2) (method 1). **d, e** $g(\hbar\omega, x)$ of CsPbBr$_3$ nanosheets without/with a PUA waveguide under 0.14 μJcm$^{-2}$ excitation is shown, respectively
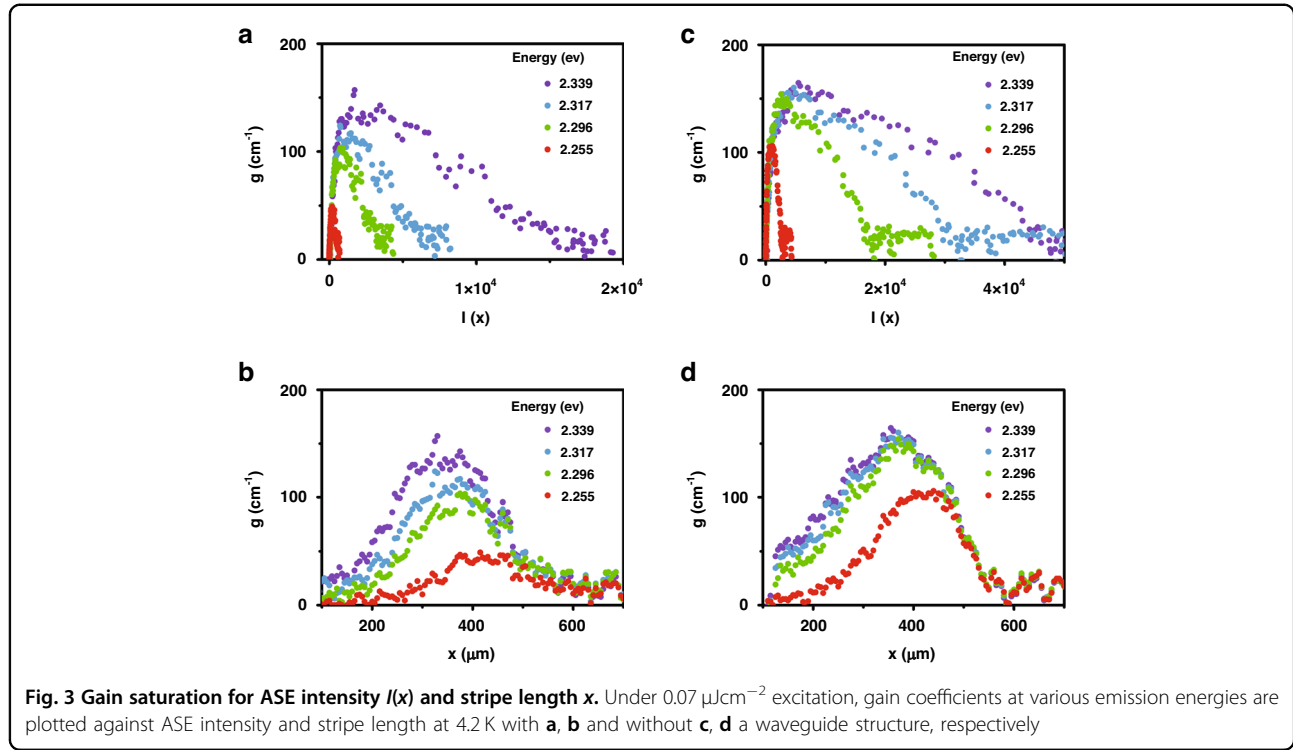
Suppose Eq. (2) is still valid up to $2x$, the gain coefficient at a selected emission energy $\hbar\omega$ can be calculated by the ratio $I(2x)$ to $I(x)$ as:

$$g(\hbar\omega) = \frac{1}{x}\ln\left(\frac{I(\hbar\omega, 2x)}{I(\hbar\omega, x)} - 1\right) \qquad (3)$$

When compared with the fitting method of Eq. (2), which needs a number of tedious iteration processes to obtain optimum parameters, the calculation method using Eq. (3) is very convenient. However, uncertainties are unavoidable in both the fitting (Eq. (2)) and calculation (Eq. (3)) although these methods are widely used to obtain gain. As the stripe length increases, gain saturation becomes significant[26]. As a result, the ASE intensity $I(x)$ shows a considerable deviation from exponential growth, and the slope decreases. Therefore, a saturation length $x_s$ should be considered to apply to both Eq. (2) and (3), but the criterion for $x_s$ is quite ambiguous, as it also depends on emission energy. Therefore, the spectral dependence of $x_s$ can modify the retrieved gain spectrum.

Additionally, the one-dimension approximation is no longer valid when the stripe length becomes comparable to the stripe width ($\sim$50 μm). In this case, the amplification is inefficient ($g \sim 0$), and the ASE intensity shows a linear increase with stripe length $I(x) \sim J_{sp}\Omega x$ up to a threshold length ($x_{th}$). It is also difficult to define the position of $x = 0$ due to laser diffraction, whereby an offset signal $I_{off}$ is observed. Therefore, Eq. (2) needs to be modified with $x_{th}$ and $I_{off}$, i.e., $I(x) = \frac{J_{sp}\Omega}{g}(\exp[g(x - x_{th})] - 1) + I_{off}$, and the fitting begins at $x_{th}$. The empirical fitting function is not a solution of the fundamental Eq. (1), and those limits are usually overlooked. Until now, most of the gain spectra reported for perovskite materials[7–13,18,19,27] were based on either Eq. (2) or Eq. (3) (method 1).

When gain saturation is considered, intensity-dependent gain $g(I)$ is usually discussed. However, it is important to notice that the stripe length dependence is associated with stripe length dependence in the VSLM, i.e., $g(I(x)) = g(x)$. Specifically, the gain saturation is related to a non-uniform distribution of photons and

**Fig. 3 Gain saturation for ASE intensity *I*(x) and stripe length *x*.** Under 0.07 μJcm$^{-2}$ excitation, gain coefficients at various emission energies are plotted against ASE intensity and stripe length at 4.2 K with **a**, **b** and without **c**, **d** a waveguide structure, respectively

carriers along the optical stripe[37]. Even if a uniform optical stripe is prepared by using a beam expander from the Gaussian intensity distribution of the laser beam[18], the carriers become depleted as the propagating ASE is amplified. At the same time, a carrier diffusion also occurs toward the depleted region. Therefore, the interplay between photons and carriers gives rise to a non-uniform carrier distribution along the stripe, and gain saturation is unavoidable in the VSLM as the stripe length increases[18,26,29,37]. Although gain saturation is often observed in the VSLM, most of them were based on the intensity dependence. Those models are not intuitive nor convenient in data analysis[37].

Based on the fundamental differential Eq. (2), we obtained the modal gain coefficient to be:

$$g(\hbar\omega, x) = \frac{\frac{dI(\hbar\omega, x)}{dx} - J_{\text{sp}}\Omega}{I(\hbar\omega, x)} \qquad (4)$$

where $\frac{dI}{dx}$ needs to be calculated from $I(x)$, and the linear slope near $x < x_{\text{th}}$ is used for $J_{\text{sp}}\Omega$. In Fig. 2c, the gain in the CsPbBr$_3$ nanosheets at 4.2 K is plotted against emission energy and stripe length $g(\hbar\omega, x)$, which looks like a gain island floating on a sea level of $g = 0$. On the upper side of Fig. 2c, the gain spectrum at $x = 330$ μm is compared with that obtained by fitting Eq. (2). Whilst the well-known analysis (method 1) provides an average gain within 500 μm, our analysis of Eq. (4) (method 2) shows a gradual gain spectrum change with stripe length. On the

right side of Fig. 2c, the stripe length dependence of the gain coefficient at 2.339 eV is also plotted. Note that the VSLM provides a net gain ($g = \gamma g_m - \alpha$). Most of the reported work on gain in perovskite materials prepared the samples by a drop-casting method. In this case, the optical confinement factor ($\gamma$) along the optical stripe is small. Compared with $g(\hbar\omega, x)$ of CsPbBr$_3$ nanosheets dropped on a PET substrate in Fig. 2d, e confirms that the PUA waveguide gives rise to a significant gain enhancement. Not only the gain coefficient but also the lateral gain area in the energy ($\hbar\omega$)-length ($x$) plane increases. This can be attributed to an increase of optical confinement factor ($\gamma$), and we have also confirmed this through a simplified simulation (Supplementary Information).

Our method with (4) is useful to study the gain saturation. In the case of inhomogeneous amplifiers, gain saturation is given $g(I) = g_0 / \sqrt{1 + I/I_{\text{sat}}}$, where the gain decreases from $g_0$ to $g_0 / \sqrt{2}$ with the saturation intensity $I_{\text{sat}}$. If the intensity dependence of the gain $g(I)$ is combined with Eq. (1), a stripe length dependence of the gain $g(x)$ can be obtained. However, experimental results are different from the theoretical predictions. Figure 3a shows $g(I)$ obtained from CsPbBr$_3$ nanosheets dropped on a PET substrate at various emission energies. Because the ASE intensity $I(x)$ was measured with increasing $x$, length-dependent gain $g(x)$ can also be obtained (Fig. 3b), i.e., $g(I(x)) = g(x)$. Obviously, the gain decrease for large $I$ do not fit with $(1 + I/I_{\text{sat}})^{-0.5}$, nor is the gain maximized with $g_0$ for small $I(x) \cong 0$. The small gain at short stripe lengths ($x < x_{\text{th}}$) can

be attributed to the limit of the one-dimensional model. Unless the optical stripe length is long enough compared with the stripe width, sufficient amplification is not achieved. In Fig. 3c, d, the enhanced gain coefficients with the PUA waveguide are plotted for increasing ASE intensity $g(I)$ and stripe length $g(x)$, respectively. These results show the optical confinement enhancement depends on the spectral energy. On the other hand, the gradual gain decrease beyond 450 μm is associated with carrier depletion, associated with the interplay between carriers and photons[29]. Whilst the photons are amplified toward the stripe edge, the carriers become depleted along the stripe. This also leads to a transient variation of the carriers and photons. Even if the excitation beam is uniform along the stripe, the carrier density becomes non-uniform. This effect becomes significant for > 450 μm giving rise to a gain saturation.

It is known that biexcitons play an essential role in the origins of intrinsic gain in CsPbBr$_3$ nanostructures[8,38]. Nevertheless, the gain lifetime of biexcitons becomes shortened as Auger recombination becomes dominant, and the biexciton Auger lifetime in CsPbBr$_3$ QDs is an order of magnitude shorter than that in colloidal CdSe QDs[22]. Surprisingly, it was found that the Auger process becomes suppressed as the confinement dimension increases from QDs (0D), nanorods (1D), and nanoplates (2D)[23,24]. In the case of 2D CsPbBr$_3$ nanoplatelets (NPLs), the Auger lifetime was known to be proportional to the lateral area[23]. Therefore, CsPbBr$_3$ nanosheets are expected to be less vulnerable to Auger effects. As the lateral size ($L = 80 \sim 300$ nm) of our CsPbBr$_3$ nanosheets is far larger than the exciton Bohr radius ($a_x \sim 3.6$ nm), a 2D free carrier model can be a possible candidate to explain the gain[11]; as the free carrier density increases in a 2D structure, the effective chemical potential increases over the band edge, determining the upper limit of the gain spectrum. The gain spectrum below the band edge also broadens as a result of various many-body effects such as carrier scattering, biexcitons, and bandgap renormalization.

However, AFM images of the CsPbBr$_3$ nanosheets (Supplementary Information) show that the thickness of a single CsPbBr$_3$ nanosheet is not constant (7–15 nm). Because the vertical thickness is far smaller than the lateral size, the confinement energy levels are dominated by the thickness. Therefore, the thickness variation of a single nanosheet gives rise to a valley-like potential energy structure, and excitons are likely to be localized near the thickness maximum. The effective localized area might be similar to that of CsPbBr$_3$ NPLs, where the area varies from 350–1100 nm$^2$. In this case, a 2D center-of-mass exciton confinement model can be considered[39], where the confinement levels are determined by a whole exciton instead of separate electrons and holes. As a result, the
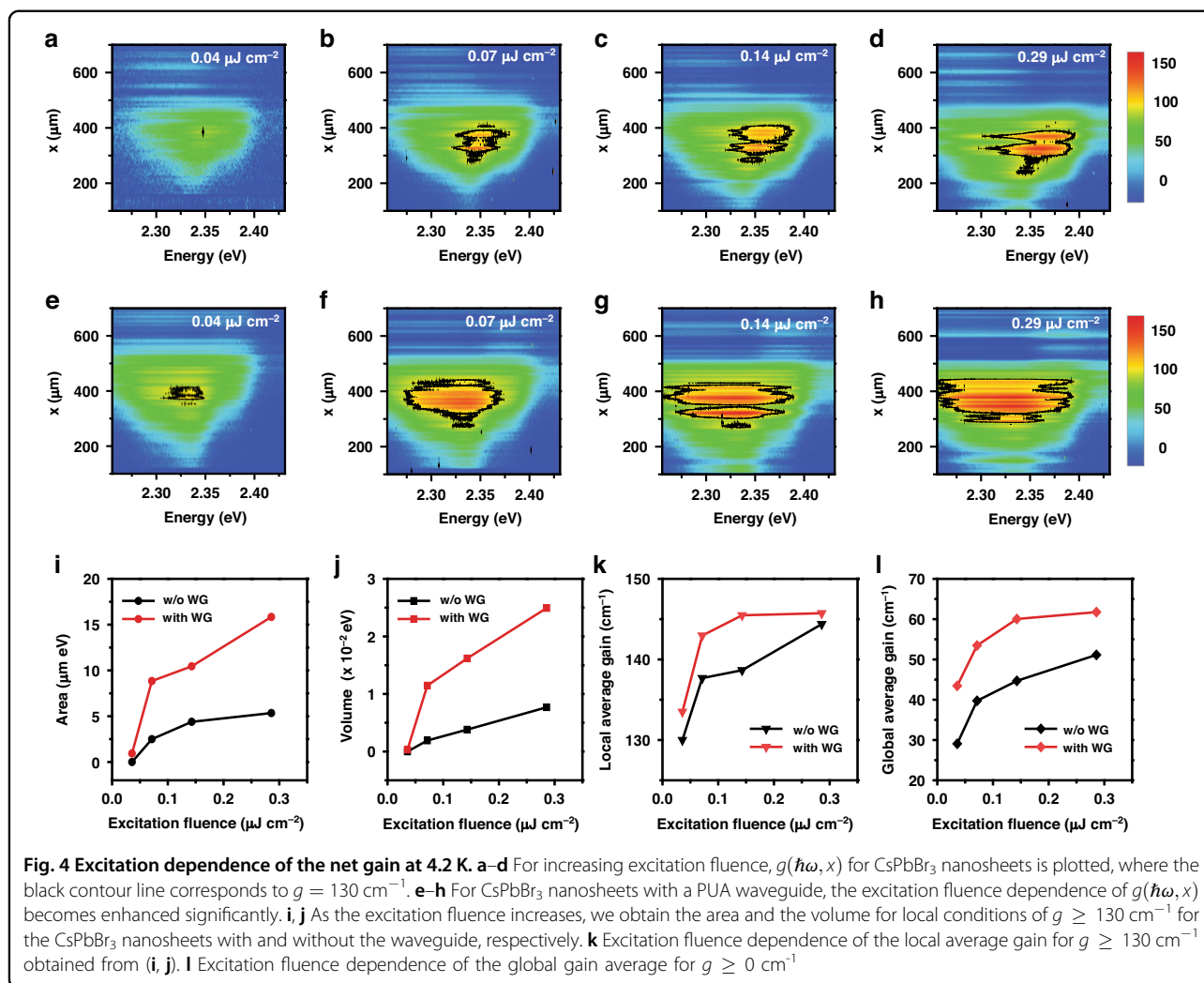
stochastic thickness variation possibly results in a broad spectral range with a different density of the states.

We should also note that our excitation fluence is smaller by two orders of magnitude than the reported threshold fluence for stimulated emission at room temperature. This difference can be attributed to the large repetition rate (80 MHz) of our laser pulses (140 fs) and the low temperature (4.2 K). Because the time interval between laser pulses (~12.5 ns) corresponding to 80 MHz is shorter than emission lifetime, the residual carriers can accumulate in a similar manner to quasi-continuous excitation. We found the threshold fluence at 4.2 K is smaller by one order of magnitude compared to that at room temperature (~2 μJcm$^{-2}$)[40].

We have also investigated the excitation dependence of the gain at 4.2 K through a spectrum-length contour plot $g(\hbar\omega, x)$. In Fig. 4a–d, the $g(\hbar\omega, x)$ of the CsPbBr$_3$ nanosheets on a PET substrate is shown as a function of increasing excitation fluence up to 0.29 μJ/cm$^2$. In Fig. 4e–h, the $g(\hbar\omega, x)$ of the CsPbBr$_3$ nanosheets with a PUA waveguide is shown again as a function of fluence. Compared with the $g(\hbar\omega, x)$ of CsPbBr$_3$ nanosheets without a PUA waveguide (Fig. 4a–d), both the vertical gain magnitude and the lateral energy-length area for the $g \geq 130$ cm$^{-1}$ show a significant increase due to the increased optical confinement factor. In addition, the gain contour shows periodic patterns along length. Although gain oscillations were observed in a noise level (Fig. 3d), the periodic feature in the large gain range becomes significant for increasing excitation. This result is possibly associated with mode propagation in the waveguide structure (Supplementary Information).

As the excitation grows, the gain spectrum usually broadens. When gain saturation becomes involved in the VSLM, the available stripe length for $g > 0$ also needs to be analyzed. We have introduced an area in the energy-length plane. For example, considering the reference contour line of $g = 130$ cm$^{-1}$, which is the maximum gain coefficient for our CsPbBr$_3$ nanosheets under 0.04 μJ/cm$^2$ excitation, the area of $g \geq 130$ cm$^{-1}$ in the energy-length plane can be obtained ($\iint d\hbar\omega dx$). In Fig. 4i, the excitation dependence of the local area for the reference $g \geq 130$ cm$^{-1}$ is plotted. For CsPbBr$_3$ nanosheets without a PUA waveguide, the local area shows a logarithmic increase with excitation fluence. With a PUA waveguide, both the spectral width and the available length for $g \geq 130$ cm$^{-1}$ increase, resulting in a significant increase in the local area.

Furthermore, we calculated the local volume $\iint g(\hbar\omega, x) d\hbar\omega dx$, where the two-dimensional gain is integrated within the area for $g \geq 130$ cm$^{-1}$. In Fig. 4j, the calculated local volume of CsPbBr$_3$ nanosheets is shown for increasing excitation fluence. Whilst the increase of the local area saturates (Fig. 4i), the local volume shows a linear increase with excitation fluence. With a PUA waveguide, the local volume increases. Given this area and
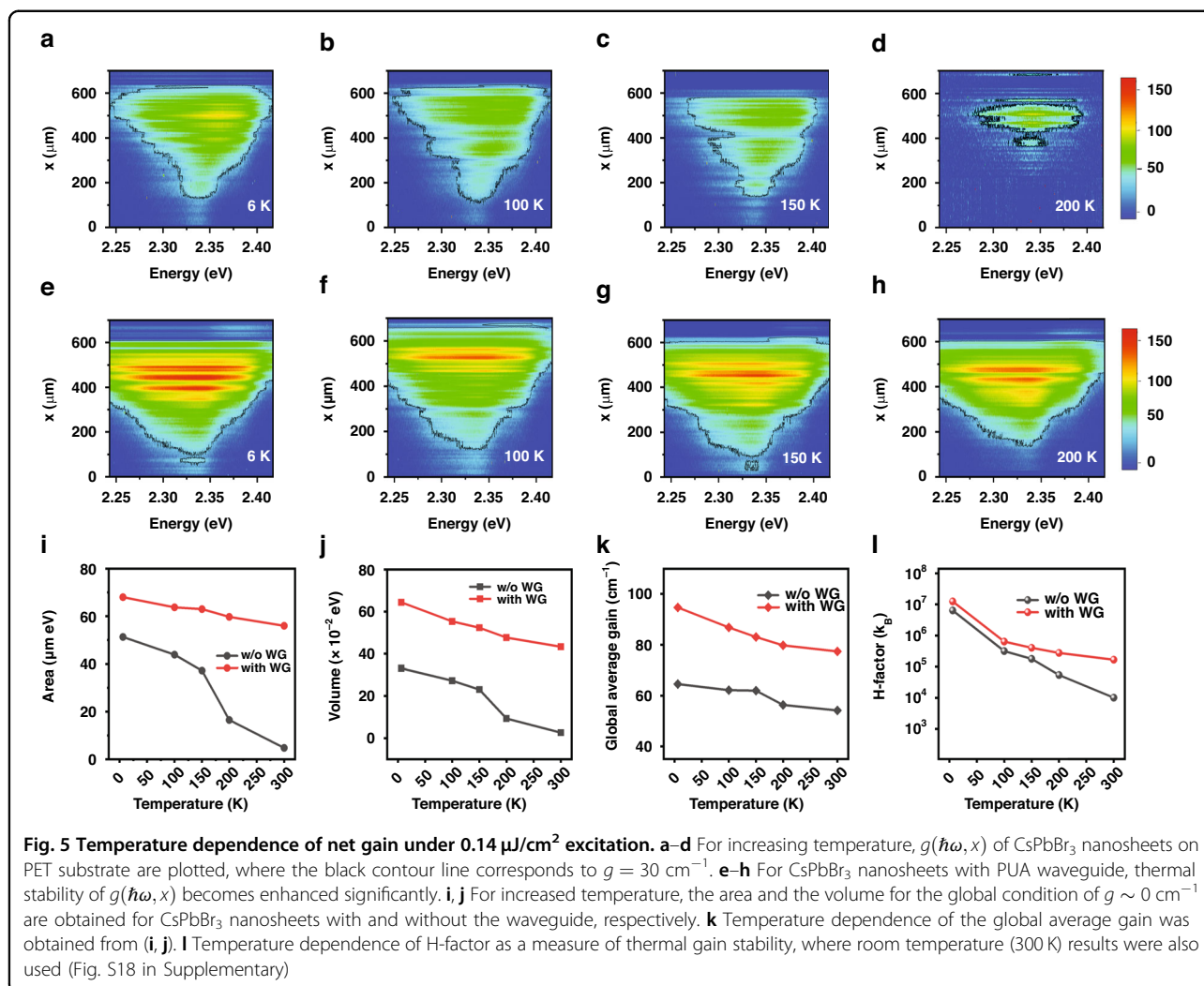
**Fig. 4 Excitation dependence of the net gain at 4.2 K. a–d** For increasing excitation fluence, $g(\hbar\omega, x)$ for CsPbBr$_3$ nanosheets is plotted, where the black contour line corresponds to $g = 130$ cm$^{-1}$. **e–h** For CsPbBr$_3$ nanosheets with a PUA waveguide, the excitation fluence dependence of $g(\hbar\omega, x)$ becomes enhanced significantly. **i, j** As the excitation fluence increases, we obtain the area and the volume for local conditions of $g \geq 130$ cm$^{-1}$ for the CsPbBr$_3$ nanosheets with and without the waveguide, respectively. **k** Excitation fluence dependence of the local average gain for $g \geq 130$ cm$^{-1}$ obtained from (**i, j**). **l** Excitation fluence dependence of the global gain average for $g \geq 0$ cm$^{-1}$

volume, we can calculate the local average gain. As shown in Fig. 4k, the excitation dependence of the local average gain for CsPbBr$_3$ nanosheets with and without a PUA waveguide are compared. This analysis might be useful to evaluate a gain medium when a cut-off gain threshold is present for lasing operation.

Similarly, a global ($g \geq 0$ cm$^{-1}$) gain average can also be obtained, where the whole area and volume are included for $g \geq 0$ cm$^{-1}$. In Fig. 4l, the global average gain for CsPbBr$_3$ nanosheets with and without a PUA waveguide are compared for increasing excitation fluence, where both show a similar logarithmic increase. In the case of a 2D gain medium, the excitation dependence of the gain is known to be $\sim g_0(1 + \ln(I/I_{th}))$, where the gain con- verges to $g_0$ near the threshold excitation power $I_{th}$[41]. Therefore, Fig. 4l supports a 2D model. In the presence of a PUA waveguide, the global gain also shows a significant enhancement compared to the local gain. Whilst PL is associated with the relaxation and transfer of excited carrier population, gain is governed by the density of states, whereby the population inversion

density is determined. It was known that the PL spectrum of CsPbBr$_3$ nanostructures is dominated by the defect states of Br vacancies and surface states, and the energy levels located below and above the exciton state were estimated by the thermal activation energy[42–45]. Together with the crystal disorder, the spatial inhomogeneity of nanosheet thickness also results in localized states (Supplementary Information). Consequently, the gain of CsPbBr$_3$ nanostructures is expected to appear with a large spectrum width (~20 meV). The defect states are distributed spatially in a stochastic manner and strongly localized. Unless stripe length is long enough, consecutive amplification of the localized states is inhibited by the absorption loss in the stripe. Likewise, the gain of the localized states develops as excitation increases. Those features are seen in the excitation dependence of $g(\hbar\omega, x)$ at 4.2 K (Fig. 4); the gain spectrum width becomes increased with increasing stripe length up to ~450 μm, resulting in an area increase in the energy-length plane.

The gain of the localized states is also sensitive to temperature, but temperature-dependent gain is reported

**Fig. 5 Temperature dependence of net gain under 0.14 µJ/cm² excitation. a–d** For increasing temperature, $g(\hbar\omega, x)$ of CsPbBr₃ nanosheets on PET substrate are plotted, where the black contour line corresponds to $g = 30$ cm⁻¹. **e–h** For CsPbBr₃ nanosheets with PUA waveguide, thermal stability of $g(\hbar\omega, x)$ becomes enhanced significantly. **i, j** For increased temperature, the area and the volume for the global condition of $g \sim 0$ cm⁻¹ are obtained for CsPbBr₃ nanosheets with and without the waveguide, respectively. **k** Temperature dependence of the global average gain was obtained from (**i, j**). **l** Temperature dependence of H-factor as a measure of thermal gain stability, where room temperature (300 K) results were also used (Fig. S18 in Supplementary)

rarely. Most of the temperature dependence in CsPbBr₃ nanostructures was reported in terms of the PL spectrum. Because the valence band maximum of CsPbBr₃ is determined by the hybridization between the $4p$ orbital of Br and the $6s$ orbital of Pb, lattice expansion reduces the hybridization between the two orbitals, resulting in a bandgap increase with temperature[46]. Additionally, localized defect states become activated, and the carrier-phonon interactions becomes enhanced. Consequently, the gain deteriorates with a spectral shift as the temperature increases.

Despite the localized states of crystal disorder and thickness inhomogeneity, perovskite materials were known to show extreme flexibility, whereby the so-called dynamic disorder occurs in a picosecond time scale[47]. As a result, the diffusion lengths of free carriers and excitons become extended up to several micrometers. This explains the efficient transport of perovskites despite defects and localized states. Therefore, the two-

dimensional center-of-mass confined excitons and the localized states coexist in the broad spectrum of perovskite nanosheets (Fig. S11 in Supplementary Information).

Our gain contour map $g(\hbar\omega, x)$ is useful for evaluating thermal stability. In Fig. 5a–d, the $g(\hbar\omega, x)$ of the CsPbBr₃ nanosheets on a PET substrate is shown for increasing temperature from 6 K up to 200 K, which is comparable with the LO-phonon energy of CsPbBr₃ (19 meV)[43]. The $g(\hbar\omega, x)$ of the CsPbBr₃ nanosheets with a PUA waveguide (Fig. 5e–h) was also obtained for comparison. Given the global gain condition of $g \sim 0$ cm⁻¹, the area (Fig. 5i) and the volume (Fig. 5j) were obtained in the energy-length plane for increasing temperature. In Fig. 5k, temperature dependence of the global average gains was compared with and without a PUA waveguide, respectively.

To quantify thermal gain stability, H-factor was also obtained by devising the global gain volume by temperature. In Fig. 5l, temperature dependence of the

H-factor is shown in units of the Boltzmann constant ($k_B$). Gain deteriorates with increased temperature but decrease of the H-factor is relatively suppressed when the waveguide structure is used. With a PUA waveguide, we found that not only the gain is enhanced but also the temperature stability improves significantly[44,45]. A possible reason would be increased thermal conduction via the PUA waveguide. It is noticeable that the channel width (~20 μm), where CsPbBr$_3$ nanosheets are stacked, and the wall width (~20 μm) of the PUA waveguide were designed intentionally with respect to the width of an optical stripe length (~50 μm). When an optical stripe is located at the optimum position, only a single channel is excited within the two side walls. Therefore, an efficient heat dissipation may occur along the wall, whereby thermal gain quenching becomes suppressed.

## Discussion

We have found that a patterned waveguide structure enhances both gain and thermal stability due to the increased optical confinement and heat dissipation. By excitation and temperature dependence of gain contour $g(\hbar\omega, x)$ in the energy-length plane, the gain origins in CsPbBr$_3$ nanosheets were attributed to the 2D center-of-mass confined excitons and the localized states arising from the inhomogeneity of thickness and the defect states.

## Materials and methods
### Materials

Lead bromide (PbBr$_2$, 99.999% trace metals basis), cesium carbonate (Cs$_2$CO$_3$, reagentPlus, 99%), 1-octadecene (ODE, technical grade, 90%), oleylamine (OLA, 70%), oleic acid (OA, 90%), octanoic acid (OctAc, 99%), octylamine (OctAm, 99%), hexane (anhydrous, 95%), and Molecular sieves, 4 ˚A were purchased from Sigma-Aldrich. PUA resin was supplied by Min- uta Technology. AZ 9260 was obtained from AZ electronic materials. AZ 300 MIF was purchased from Merck. Sylgard 184 was supplied by Dow Corning. ODE, OA and OLA were dehydrated using molecular sieves before use, other chemicals were used as received without further purification.

### Preparation of Cs-oleate solution

The Cs-oleate solution was prepared by the method reported by Dou et al.[48], Cs$_2$CO$_3$ (0.16 g) and OA (10 ml) were loaded into 25 ml 3-neck flask and dried under vacuum at 120 °C for 50 min, and then heated under N$_2$ to 140 °C until all Cs$_2$CO$_3$ reacted with OA. Cs-oleate solution was pre-heated to 100 °C before injection.

### Synthesis of CsPbBr$_3$ nanosheets

ODE (10 ml), PbBr$_2$ (0.069 g), OA (0.3 ml), OLA (0.3 ml), OctAc (0.5 ml), and OctAm (0.5 ml) were loaded into 50 ml 3-neck flask and dried under vacuum for 20 min at 100 °C. After complete solubilization of the PbBr$_2$, the temperature was raised to 150 °C under N$_2$. In total, 0.8 ml of Cs-oleate solution was swiftly injected. After 20 min, the reaction was stopped by using an ice-water bath to room temperature. The crude solution was dispersed in anhydrous hexane and centrifuged at 2000 rpm for 5 min. The supernatant was discarded, and the precipitate was re-dispersed in anhydrous hexane. This isolation process was repeated again, and the supernatant was collected separately for further process.

### Preparation of line-patterned PUA substrate

In order to prepare the PDMS mold, a drop of photoresist (PR) was placed on a chrome-coated glass substrate (100 × 100 × 0.5 mm), a spin-coating process was performed at a spinning speed of 750 rpm for 30 s. The coated substrate was then soft-baked at the temperature of 110 °C for 10 min. UV radiation with 1800 mJcm$^{-2}$ illuminated the substrate placed under a patterned mask, the development was processed using a developer solution for 20 min. Rinsed with DI water, the patterned mold was completely dried on a hot plate. To fabricate a PDMS replica mold, a PDMS prepolymer with a curing agent solution was poured on the patterned mold and cured at 80 °C for 1 h. Subsequently, an appropriate amount of PUA resin was dropped on the PDMS mold to create a line-patterned substrate. Then, a PET guide film was located on the PUA resin and uniformly pressed using a roller for conformal contact between the PUA resin and the PET film. The PUA resin was then exposed to UV light ($\lambda = 365$ nm). After fully curing, the PDMS mold was carefully detached from patterned PUA substrate.

### Capillary-directed self-assembly of perovskite nanosheets

The line-patterned PUA substrate (2 × 2 cm$^2$) was used without an additional cleaning process. The deposition process for the CsPbBr$_3$ nanosheets on the line-patterned substrate was conducted on a hot plate set at 60 °C to facilitate the evaporation of the volatile solvent (i.e., hexane) and the deposition. Next, an upper blade was installed at a 30° angle, and the colloidal perovskite solution was injected in a confined geometry containing the upper blade and the lower substrate. A trapped meniscus was formed by capillary force in this restricted geometry, and 20 cycles of one-way motion were performed at a speed of 2.5 mm/s by a computer-controlled translation stage. A uniformly stacked perovskite nanosheet film layer on PUA microfluidic channels was obtained through the repetitive capillary-directed self-assembly process. After the deposition process, the multi-stacked perovskite nanosheets on a patterned substrate were stored in a vacuum desiccator for further measurement and experiments.

## Characterization of CsPbBr₃ nanosheets and line-patterned substrate

The synthesized $CsPbBr_3$ nanosheets were observed by TEM (TALOS, F200X) under an acceleration voltage of 200 kV to confirm their morphologies. HRTEM and SAED analyses also were performed on transmission electron microscope (TALOS, F200X). The thickness of the $CsPbBr_3$ nanosheets was measured by an AFM (Park systems, NX10). The UV-Vis absorption spectra were measured on an Evolution 220 UV-Visible Spectrophotometer. The PL spectra were recorded by a Fluorescence Spectrophotometer (Hitachi, F-7000). The multistacked perovskite nanosheets on the patterned PUA substrate were observed by SEM (Gemini, SUPRA 40 VP) and Digital Microscope (CELENA®S Digital Microscope). For optical gain measurement, frequency-doubled 400 nm pulses (140 fs duration) were used, which are operating at 80 MHz repetition rate, and the fundamental pulses of 800 nm are pumped by 18 W continuous laser.

### Author details
¹Department of Opto & Cogno Mechatronics Engineering, RCDAMP, Pusan National University, Busan 46241, Republic of Korea. ²Department of Nano-Fusion Technology, Pusan National University, Busan 46241, Republic of Korea. ³Clarendon Laboratory, Department of Physics, University of Oxford, Oxford OX1 3PU, UK

### Author contributions
K.K. and S.W.H. came up with ideas and designed experiments. G.E.C. synthesized perovskite nanosheets and fabricated waveguide. M.M. and M.W.K. performed optical gain measurements, and I.K., M.M., M.K., K.K., and R.A.T. participated in data analysis, and T.J. and S.K. calculated theoretical simulation. All authors discussed the results and commented on the manuscript.

### Data availability
The data that support these findings are available from the corresponding author upon request. Source data of all figures are provided with this paper.

### Conflict of interest
The authors declare no competing interests.

### References
1. Li, Y. X. et al. Advances in metal halide perovskite nanocrystals: synthetic strategies, growth mechanisms, and optoelectronic applications. *Mater. Today* **32**, 204–221 (2020).
2. Mao, Y. L. et al. Enhanced amplified spontaneous emission from all-inorganic perovskite thin films by composition engineering. *Adv. Opt. Mater.* **10**, 2201845 (2022).
3. Kojima, A. et al. Organometal halide perovskites as visible-light sensitizers for photovoltaic cells. *J. Am. Chem. Soc.* **131**, 6050–6051 (2009).
4. Jiang, Q. et al. Surface reaction for efficient and stable inverted perovskite solar cells. *Nature* **611**, 278–283 (2022).
5. Tan, Z. K. et al. Bright light-emitting diodes based on organometal halide perovskite. *Nat. Nanotechnol.* **9**, 687–692 (2014).
6. Kim, J. S. et al. Ultra-bright, efficient and stable perovskite light-emitting diodes. *Nature* **611**, 688–694 (2022).
7. Xing, G. C. et al. Low-temperature solution-processed wavelength-tunable perovskites for lasing. *Nat. Mater.* **13**, 476–480 (2014).
8. Yakunin, S. et al. Low-threshold amplified spontaneous emission and lasing from colloidal nanocrystals of caesium lead halide perovskites. *Nat. Commun.* **6**, 8515 (2015).
9. Pourdavoud, N. et al. Room-temperature stimulated emission and lasing in recrystallized cesium lead bromide perovskite thin films. *Adv. Mater.* **31**, 1903717 (2019).
10. Lin, X. H. et al. Vapor phase growth of centimeter-sized band gap engineered cesium lead halide perovskite single-crystal thin films with color-tunable stimulated emission. *Adv. Funct. Mater.* **33**, 2210278 (2023).
11. Geiregat, P. et al. Using bulk-like nanocrystals to probe intrinsic optical gain characteristics of inorganic lead halide perovskites. *ACS Nano* **12**, 10178–10188 (2018).
12. Wang, S. et al. Stable, strongly emitting cesium lead bromide perovskite nanorods with high optical gain enabled by an intermediate monomer reservoir synthetic strategy. *Nano Lett.* **19**, 6315–6322 (2019).
13. Tian, J. Y. et al. Perovskite quantum dot one-dimensional topological laser. *Nat. Commun.* **14**, 1433 (2023).
14. Kang, C. H. et al. High-speed colour-converting photodetector with all-inorganic $CsPbBr_3$ perovskite nanocrystals for ultraviolet light communication. *Light Sci. Appl.* **8**, 94 (2019).
15. Ding, N. et al. A novel approach for designing efficient broadband photodetectors expanding from deep ultraviolet to near infrared. *Light Sci. Appl.* **11**, 91 (2022).
16. Sutton, R. J. et al. Bandgap-tunable cesium lead halide perovskites with high thermal stability for efficient solar cells. *Adv. Energy Mater.* **6**, 1502458 (2016).
17. Jiang, G. C. et al. Highly luminescent and water-resistant $CsPbBr_3$- $CsPb_2Br_5$ perovskite nanocrystals coordinated with partially hydrolyzed poly(methyl methacrylate) and polyethylenimine. *ACS Nano* **13**, 10386–10396 (2019).
18. Alvarado-Leaños, A. L. et al. Optical gain of lead halide perovskites measured via the variable stripe length method: what we can learn and how to avoid pitfalls. *Adv. Opt. Mater.* **9**, 2001773 (2021).
19. Tatarinov, D. A. et al. High-quality $CsPbBr_3$ perovskite films with modal gain above 10 000 cm⁻¹ at room temperature. *Adv. Opt. Mater.* **11**, 2202407 (2023).
20. Castañeda, J. A. et al. Efficient biexciton interaction in perovskite quantum dots under weak and strong confinement. *ACS Nano* **10**, 8603–8609 (2016).
21. Ahn, N. et al. Electrically driven amplified spontaneous emission from colloidal quantum dots. *Nature* **617**, 79–85 (2023).
22. Li, H. S. et al. Low-dimensional inorganic tin perovskite solar cells prepared by templated growth. *Angewandte Chemie Int. Edn.* **60**, 16330–16336 (2021).
23. Li, Q. Y. et al. Size- and morphology-dependent auger recombination in $CsPbBr_3$ perovskite two-dimensional nanoplatelets and one-dimensional nanorods. *Nano Lett.* **19**, 5620–5627 (2019).
24. Li, Q. Y. & Lian, T. Q. Area- and thickness-dependent biexciton auger recombination in colloidal CdSe nanoplatelets: breaking the "universal volume scaling law". *Nano Lett.* **17**, 3152–3158 (2017).
25. Sun, P. Z. et al. Single-layer nanosheets with exceptionally high and anisotropic hydroxyl ion conductivity. *Sci. Adv.* **3**, e1602629 (2017).
26. Negro, L. D. et al. Applicability conditions and experimental analysis of the variable stripe length method for gain measurements. *Opt. Commun.* **229**, 337–348 (2004).
27. Zeng, X. et al. Achieving low threshold and high optical gain amplified spontaneous emission in MAPbI₃ perovskite films via symmetric waveguide effect. *Adv. Opt. Mater.* **10**, 2201328 (2022).
28. Shaklee, K. L. & Leheny, R. F. Direct determination of optical gain in semiconductor crystals. *Appl. Phys. Lett.* **18**, 475–477 (1971).
29. Goebel, E. O., Hildebrand, O. & Lohnert, K. Wavelength dependence of gain saturation in GaAs lasers. *IEEE J. Quantum Electron.* **13**, 848–854 (1977).
30. Zhang, M. Z. et al. Growth and characterization of all-inorganic lead halide perovskite semiconductor $CsPbBr_3$ single crystals. *CrystEngComm* **19**, 6797–6803 (2017).

31. Protesescu, L. et al. Nanocrystals of cesium lead halide perovskites (CsPbX$_3$, X = Cl, Br, and I): novel optoelectronic materials showing bright emission with wide color gamut. *Nano Lett.* **15**, 3692–3696 (2015).

32. Lv, L. F. et al. Generalized colloidal synthesis of high-quality, two-dimensional cesium lead halide perovskite nanosheets and their applications in photo-detectors. *Nanoscale* **8**, 13589–13596 (2016).

33. Shamsi, J. et al. Colloidal synthesis of quantum confined single crystal CsPbBr$_3$ nanosheets with lateral size control up to the micrometer range. *J. Am. Chem. Soc.* **138**, 7240–7243 (2016).

34. Jun, S. W. et al. Full-color laser displays based on optical second-harmonic generation from the thin film arrays of Selenium nanowires. *ACS Photonics* **9**, 368–377 (2022).

35. Hong, S. W. et al. Directed self-assembly of gradient concentric carbon nanotube rings. *Adv. Funct. Mater.* **18**, 2114–2122 (2008).

36. Lee, J. et al. Enabling the selective detection of endocrine-disrupting chemicals via molecularly surface-imprinted "Coffee Rings". *Biomacromolecules* **22**, 1523–1531 (2021).

37. Lange, C. et al. The variable stripe-length method revisited: improved analysis. *Appl. Phys. Lett.* **91**, 191107 (2007).

38. Zhao, W. et al. Optical gain from biexcitons in CsPbBr$_3$ nanocrystals revealed by two-dimensional electronic spectroscopy. *J. Phys. Chem. Lett.* **10**, 1251–1258 (2019).

39. Jang, J. et al. Excitation and temperature dependence of the broad gain spectrum in GaAs/AlGaAs quantum rings. *Appl. Phys. Lett.* **117**, 213101 (2020).

40. Liang, Y. et al. Solvent recrystallization-enabled green amplified spontaneous emissions with an ultra-low threshold from pinhole-free perovskite films. *Adv. Funct. Mater.* **31**, 2106108 (2021).

41. Haug, H. & Koch, S. W. *Quantum Theory of the Optical and Electronic Properties of Semiconductors*, 5th edn. (World Scientific Publishing Company, 2009).

42. Morello, G. et al. Temperature-dependent amplified spontaneous emission in CsPbBr$_3$ thin films deposited by single-step RF-magnetron sputtering. *Nanomaterials* **13**, 306 (2023).

43. Pashuk, I. P. et al. Exciton absorption, luminescence and resonance Raman scattering in CsPbCl$_3$ and CsPbBr$_3$ crystals at low temperatures. *Soviet Phys. Solid State* **23**, 2162–2165 (1981).

44. Balena, A. et al. Temperature dependence of the amplified spontaneous emission from CsPbBr$_3$ nanocrystal thin films. *J. Phys. Chem. C* **122**, 5813–5819 (2018).

45. De Giorgi, M. L. et al. Amplified spontaneous emission properties of solution processed CsPbBr$_3$ perovskite thin films. *J. Phys. Chem. C* **121**, 14772–14778 (2017).

46. Saran, R. et al. Giant bandgap renormalization and exciton–phonon scattering in perovskite nanocrystals. *Adv. Opt. Mater.* **5**, 1700231 (2017).

47. Munson, K. T. et al. Dynamic disorder dominates delocalization, transport, and recombination in halide perovskites. *Chem* **4**, 2826–2843 (2018).

48. Dou, L. T. et al. Atomically thin two-dimensional organic-inorganic hybrid perovskites. *Science* **349**, 1518–1512 (2015).